Flow (2022), **0** E1
doi:10.4153/xxxx

RESEARCH ARTICLE

Supplementary Information: Leidenfrost Flows : instabilities and symmetry breakings

E. Yim[1], A. Bouillant[2,3], D. Quéré[2,3], F. Gallaire[1]

Received xx xxx xxxx

We enclose here supplemental data, figures and movies, following the development of the accompanying paper.

1. Captions of the movies:

Movie S1

Surface flows of a Leidenfrost drop viewed from the top throughout its life played in real time. A puddle ($R \approx 3.5$ mm) is initially deposited in a groove heated at T = 350°C. Hydrophobic tracers standing at the interface draw convective chaotic patterns that tend to organize into a 4-cell symmetric structure. For $R \approx 1.8$ mm, drop vibrations intensify and the symmetry breaks. Then, the drop starts to roll. Rolling persists until tracers saturate and form a static solid shell at the surface. The white bar indicates 2 mm.

Movie S2

Side view of a water drop levitating on a plate heated at 350°C observed with an infrared camera using a calibration range from −40°C to 150°C, only suitable for water, and not brass. The bar indicates 5 mm, and the movie is sped up by a factor 3.2, while the right-handed lateral color bar gives access to the surface temperature of the drop.

2. Heat transfer modelling on $\partial\Omega_F$

The heat transfers on the drop interface (on $\partial\Omega_F$) are provided by the convection and conduction to the surrounding air, and also by the evaporation, which cools down the liquid as sketched in figure 3 of our manuscript. We write the conductive heat flux as j_k, the convective heat flux j_c, and the evaporative-driven cooling flux as j_e (Bergman *et al.*, 2011). At equilibrium, these heat fluxes must balance[1]

$$j_k = j_c + j_e. \tag{1}$$

The conductive and convective heat fluxes at the interface are respectively modelled with Fourier's diffusive law and with the semi-empirical Newton's law for convection. Ultimately, the evaporation-driven cooling term is proportional to the energy required to produce a mass flux n' at the interface.

[1]We neglect here the radiative heat flux j_r, which, according to Stefan-Boltzmann law, scales as $\sigma_{SB}\,\epsilon_r T^4$, where $\sigma_{SB} = 5.67\cdot10^{-8}$ W/m^2/K^4 is the Stefan's constant and $\epsilon_r \approx 1$ the body emissivity. Indeed, the typical convective heat transfer coefficient h_c for liquid subjected to forced convection is 10^4 W/m^2/K, such that $j_r/j_c \ll 1$.

Denoting the latent heat for vaporization as $\mathcal{L}$, it comes $j_e = n'\mathcal{L}$. The respective contributions are thus

$$j_k = -(k \cdot \nabla T)\mathbf{n}, \tag{2}$$

$$j_c = h_c(T - T_a), \tag{3}$$

$$j_e = n'\mathcal{L}, \tag{4}$$

where k is the liquid thermal conductivity, $\mathbf{n}$ the normal unit vector, h_c the convective heat transfer coefficient and T_a the ambient air temperature. The evaporation rate n' is the mass flux per unit area of water molecule transferring from a liquid to a gas state across the drop interface, which can be expressed as:

$$n' = h_m(s_a(T_F) - \phi_{\mathrm{RH}} s_a(T_a)), \tag{5}$$

where h_m is the evaporative heat transfer coefficient, s_a the saturation vapor density and ϕ_{RH} the relative humidity. The saturation vapor density is strongly dependent on the temperature and it increases approximately as $\sim T^3$, which accelerates the evaporation cooling at high temperature.

In order to determine h_m, we introduce the Sherwood number Sh, the dimensionless concentration gradient at the interface $\partial\Omega_F$, commonly used in transport phenomena to compare convective mass transfer to diffusion mass rate. Denoting D_{va} as the water vapor-air binary mass diffusivity and H the characteristic distance on which the transfer is operated, the evaporative heat transfer coefficient h_m can be estimated using the the mass transfer correlation law as

$$h_m = Sh\frac{D_{va}}{H}. \tag{6}$$

The Sherwood number can be approximated using Ranz-Marshall correlation which related the convective heat and mass transfers around spherical drop (Ranz & Marshall, 1952; Bergman *et al.*, 2011) :

$$Sh = 2 + 0.6\,(Re_a)^{1/2}\,(Sc_a)^{1/3}\,, \tag{7}$$

where Re_a is the Reynolds number associated to the air flow generated around the drop owing to thermal convection and Sc_a the Schmidt number. The Re_a can be determined using the relation of the kinetic energy (due to the convective flow in air with typical velocity V_a) and the potential energy (due to thermobuoyant effect, operating at the characteristic vertical length L_a):

$$\rho_a V_a^2 \approx g\beta_a(T_p - T_\infty)L_a, \tag{8}$$

reads

$$Re_a = \frac{L_a V_a}{\nu_a} = \sqrt{\frac{g\beta_a L_a^3}{\rho_a \nu_a^2}} \sim \sqrt{\frac{Ra_a}{Pr_a}}. \tag{9}$$

where Ra_a is the Rayleigh number defined as

$$Ra_a = \frac{g\beta_a(T_p - T_a^\infty)L_a^3}{\nu_a \kappa_a}, \tag{10}$$

and Pr_a the Prandtl number in air, which is the ratio of the momentum and thermal diffusivities:

$$Pr_a = \frac{\nu_a}{\kappa_a}. \tag{11}$$

The Schmidt number Sc_a for the ambient air is defined as the ratio of the momentum and mass diffusivities

$$Sc_a = \frac{\nu_a}{D_{va}}. \tag{12}$$

Those dimensionless numbers are evaluated by the tabulated physical properties for water and gas, and their variations with respect to the temperature T as summarized in table 1. All the physical and semi-empirical parameters relative to water, vapor, air and their interface, are extracted from the literature (e.g. EngineeringToolBox (2001)) at the lumped mean temperatures of the phase they refer to (at roughly 80–100°C for water and $(T_p - T_\infty)/2 \approx 100$°C for air). We thus get $Pr_a = 0.71$. Assuming that air and vapor behave like ideal gas and considering temperature variations from 80°C to 100°C for the air, we finally get $Re_a \simeq 125$ and $Sc_a \simeq 0.60$, so that, according to the relation (7), $Sh = 7.8$. Hence, the evaporative heat transfer coefficient h_m can be deduced from (6) $h_m = 0.07$ m/s.

Regarding now the contribution of thermal convection j_c, we use a similar approach to assess the convective heat transfer coefficient h_c which can be represented by the Nusselt number. The Nusselt number Nu_a is defined as the ratio between convective to conductive heat transfers in air at the drop vicinity:

$$Nu_a = \frac{h_c H}{k_a}. \tag{13}$$

As it represents the dimensionless temperature gradient at the interface, it plays an analogous role than the Sherwood number for mass transfer. From this analogy, the Ranz-Marshall correlation for heat convection reads as

$$Nu_a = 2 + 0.6(Re_a)^{1/2}(Pr_a)^{1/3}. \tag{14}$$

We thus find $Nu_a \approx 8$, which means that heat convection in air dominates heat conduction around the drop. To evaluate the convective heat exchange from the air to the droplet interface, Biot number (Bi) is introduced, which compares the heat transfer resistance inside the drop (of convective nature) to the resistance to heat exchange at its surface (of conductive nature), expressed in terms of the thermal conductivity of air and of water and of the Nusselt number related to air:

$$Bi = \frac{h_c H}{k} = \frac{k_a}{k} Nu_a = 0.4. \tag{15}$$

We then have $h_c = 63$ W/m^{2}K. We note that Tam *et al.* (2009) used the effective Biot number from the effective heat transfer coefficient which is the sum of the convective and evaporative heat fluxes divided by the temperature difference between ambient and the droplet surface temperature $(T - T_a)$.

3. Inner drop temperature

As a complement (and calibration) to the surface temperature mapping with a side-view infrared camera, a 100 μm radius thermocouple is inserted to a height z into a drop (the reference $z = 0$ being on the substrate and H being the drop height) to provide the liquid inner temperature T. This measurement is intrusive and does not permit the access to temperature close to the boiling point, as bubble nucleate on the thermocouple so as the contact liquid/solid is lost. Nevertheless, the temperature profile displayed in figure 1, confirms the existence of vertical temperature gradient of a tens of degrees, decreasing from the drop bottom to its apex (cooled down by ambient air). The temperature inside a drop increases linearly from 88.5 ± 0.5°C at the drop apex, that is for $z/H \approx 1$, to 92.5 ± 0.5°C for $z/H \approx 0.4$, where the thermocouple dewets owing to the formation of bubbles. Extrapolating the linear fit to the drop base ($z/H \approx 0$), we expect there a temperature of 94.5 ± 0.5°C, slightly lower than the water boiling point, as shift we interpret as arising from a deviation from the linear trend close to the evaporating interface (Laplace's equation is modified by the loss term), but also as a consequence of the endothermic character of evaporation.

Variable	Symbol	Mean value
Liquid (maintained at $T \approx 100°C$)		
Density	ρ_0	$\rho_0 = 958$ kg/m^3
Thermal expansion	β_w	$\beta_w = 6.88 \cdot 10^{-4}$ m^3/kg/°C
Kinematic viscosity	ν	$\nu = 3 \cdot 10^{-7}$ m^2/s
Thermal diffusivity	κ	$\kappa = 0.17 \cdot 10^{-6}$ m^2/s
Thermal conductivity	k	$k = 0.6$ W/m/K
Liquid/air interface		
Surface tension	σ_0	58 mN/m (at $T = 100°C$)
Change in surface tension with T	σ_1	$\sigma_1 = 0.185$ mN/m/K
Evaporation latent heat	$\mathcal{L}$	$\mathcal{L}(T) = 2503 - 2.44 \times T$ kJ/kg
Convective heat transfer	h_c	$h_c = 63$ W/m^{2}K from eq.(15)
Evaporative heat transfer coefficient	h_m	$h_m \approx 0.07$ m/s from eq.(6)
Evaporative mass flux per unit area	n'	$n' \approx 0.01$kg/m^2/s from eq.(5)
Air/vapor (ideal gas at $T \approx (T_p - T_\infty)/2$)		
Kinematic viscosity	ν_a	$\nu_a = 20 \cdot 10^{-6}$ m/s
Thermal diffusivity	κ_a	$\kappa_a = 40 \cdot 10^{-6}$ m^2/s
Thermal conductivity	k_a	$k_a = 26 \cdot 10^{-3}$ W/m $\cdot$ K
Thermal expansion	β_a	$\beta_a(T) = 1/T \approx 3.5 \cdot 10^{-3}$ K^{-1}
Water vapor-air binary mass diffusivity	D_{va}	$D_{va}(T) = 4.7 \cdot 10^{-9} \times T^{3/2}$ m^2/s
Air relative humidity	ϕ_{RH}	$\phi_{\mathrm{RH}} = 0.3 - 0.2$
Saturation vapor density	s_a	$s_a(80°C) = 0.29$ kg/m^3, $s_a(100°C) = 0.59$ kg/m^3

Table 1. *Physical and semi-empirical parameters relative to water, vapor, air and their interface, involved in our analysis. Values are extracted from literature (e.g. EngineeringToolBox (2001)), and are assessed at the mean temperature of the phase they refer to. Temperature sensitivity is detailed.*

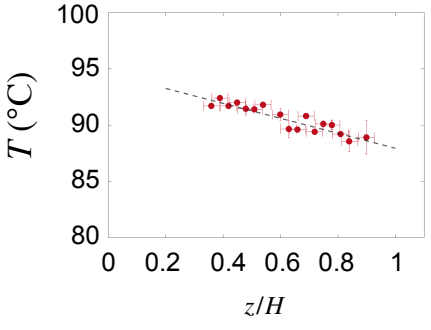

Figure 1. *Temperature T along the central vertical axis of a water drop ($R = 1.67 \pm 0.15$ mm, and $H \approx 2$ mm), obtained by lowering a thin thermocouple at a speed $\mathrm{d}z/\mathrm{d}t = -0.1$mm/s in water. The temperature difference ΔT between the top and the bottom of the drop is found to be a few degrees. At a distance $z/H \approx 0.4$, water partially dewets the thermocouple and moves away on its side, which hinders temperature measurement for $z/H < 0.4$. A linear fit of the temperature field gives $T = -6.6z/H + 94.6$, expressed in °C, drawn with a dashed line.*

4. Ambient air temperature

In order to solve the full thermal problem and to be able to prescribe the temperature at the drop free interface, we focus on the thermal boundary condition at the drop upper interface. The air around the plate is also heated and we expect its temperature to decrease as the vertical coordinate z increases. We here try to characterize the temperature field above the plate, denoted as $T_a(z)$. The attempt to use a thermocouple to access the temperature in air failed, as air flows driven by natural convection cool down the thermocouple extremity, and the temperature value read considerably fluctuates. Alternatively, a silicon wafer with thickness 500 μm, is placed above the plate heated at $T_p = 300°C$. The high value of the thermal conductivity of silicon (about 1 W/cm/K) guarantees a fast and efficient thermalization with the ambient. We use a side-viewed infrared, calibrated on silicon substrates on the desired range of temperature, to map the temperature distribution $T_a(z)$ above the plate. The measurement is carried out under the same conditions than that of the previous experiments but in the absence of a Leidenfrost drop. The presence of a Leidenfrost drop may slightly disturb the temperature field $T_a(z)$ by cooling it down.

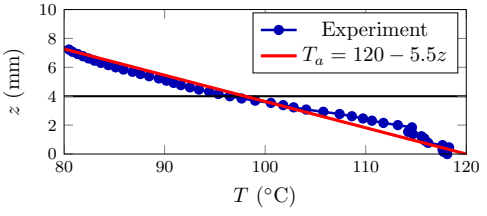

Figure 2. *Temperature of the ambient air at a distance z above a plate heated at $T_p = 300°C$, accessed with an infrared camera pointing on a highly conductive silicon wafer, in the absence of a drop. The dark horizontal line indicates $z = 4$ mm, which corresponds to the maximum height of the droplet at $t = 0$. Data are adjusted with a linear fit of equation $T_a = 120 - 5.5z$ plotted in red. Those thermal data are used as input for the heat transfer modelling in §2.*

The temperature distribution $T_a(z)$ in the air is reported in figure 2. $T_a(z)$ decreases as the distance z from the plate increases and can be approximated by the linear fit $T_a(z) = 120 - 5.5z$ which is used in the numerical modelling.

5. Effect of ambient temperature

In the experiments, various plate temperatures (from $T_s = 250°C$ to $T_s = 450°C$) showed a robust critical radius for the mode transition from $m = 2$ to $m = 1$. Numerically, the bottom temperature of the droplet is fixed to the boiling temperature thus, the change of the plate temperature does not impact on the numerical modelling. However, this variation of the plate temperature can affect the ambient air temperature which involves the heat exchange on $\partial\Omega_F$. In the manuscript, we used the experimentally measured temperature which is obtained for $T_s = 300°C$. Therefore, in this appendix, we investigate the effect of the surrounding air temperature on the stability analysis. The stability analysis is conducted for two additional air profiles as shown in figure 3: higher bottom temperature $T_a = 150 - 5z$ and smoother gradient $T_a = 120 - 3z$. Other parameters are kept the same ($\sigma_{1,\text{eff}} = 4 \cdot 10^{-5}\sigma_1$).

The stability results are depicted in figure 4. The air temperature slightly moves the critical radius of the mode transition as summarized in table 5. Compare to the results using the measured air temperature ($T_a = 120 - 5.5z$), the critical radii for higher temperature $T_a = 150 - 5z$ are increased by 0.2 mm while the one with smoother slope $T_a = 120 - 3z$ has almost no impact on the critical radii. Again, all these values fall into the experimental observation.

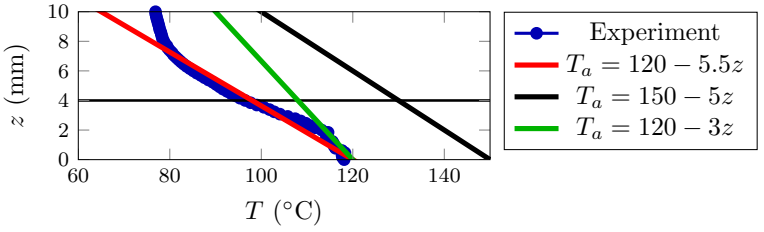

Figure 3. *Various air temperatures. The thick blue curve is experimental data. The red line what is used in the manuscript and black and green are two tested air temperatures.*

T_a	$R_{c,3\to2}$ (mm)	$R_{c,2\to1}$ (mm)
$120 - 5.5z$ (manuscript)	2.1	1.3
$150 - 5z$	2.3	1.5
$120 - 3z$	2.1	1.3

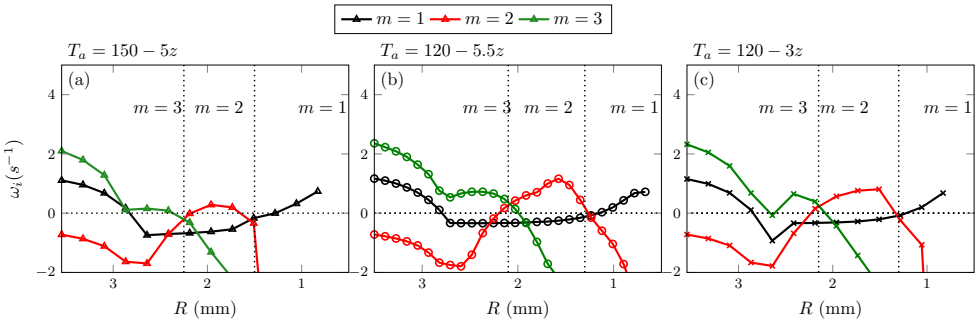

Figure 4. *(a) $T_a = 150 - 5z$ (triangle), (b) $T_a = 120 - 5.5z$ (circle) and is close to the experimental data and (c) $T_a = 120 - 3z$ (cross).*

6. Influence of the substrate temperature on the critical radius

The experiment proposed by (Bouillant *et al.*, 2018*b*) is thus reproduced in the SI (as schematized in figure 5a) for plate temperatures ranging from 250 to 450°C and we display in figure 5(b) the acceleration a of about 80 drops as a function of their radii R. Over this broad range of plate temperatures, accelerations exhibit similar jumps from about 1 mm/s^2 (in the regime where drops are flattened by gravity), up to 60 mm/s^2 below $R \sim 1$ mm (in the self-rotation and self-propelling regime) (Bouillant *et al.*, 2018*a*). The spontaneous apparition of internal rolling is robust and consistent. The onset for the transition from $m = 2$ to $m = 1$, referred as $R_{2\to1}$, is found within the interval $[1, 1.5]$ mm and weakly varies over the range of temperature explored ($T_p = [250, 450°\text{C}]$) as seen in figure 5(c).

7. Baseflow with effective Ma

As mentioned in §4 of the accompanying paper, there exist uncertainties regarding on the *real* Marangoni effect of the water interface. In this section, discuss the choice of Ma_{eff} on our results. The surface tension variation σ_1 is multiplied with a constant to have $\sigma_{1,\text{eff}} \leq \sigma_1$ then Ma_{eff} is evaluated with $\sigma_{1,\text{eff}}$ and the resulting ΔT.

Figure 6 shows the baseflow for increasing values of Ma_{eff}, for a drop with $R = 3$ mm. The amplitude of the maximum velocity increases dramatically from 5 cm/s to 5000 cm/s as Ma_{eff} is increased from

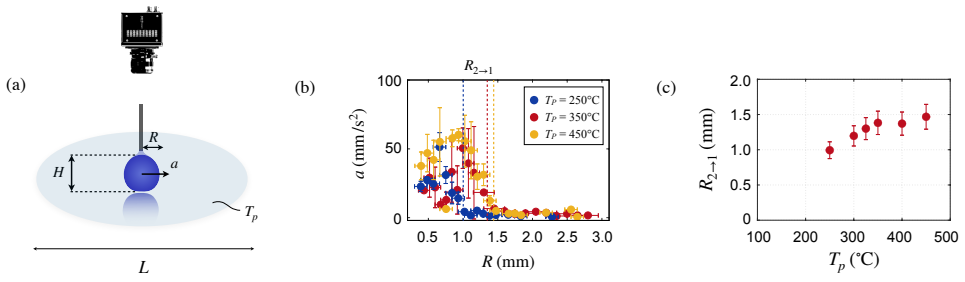

Figure 5. *Self-propulsion of Leidenfrost drops for different plate temperature T_p. (a) Schematic of the experiment described in Bouillant et al. (2018b): trajectories of about 80 drops initially at rest and with radius set by the height of the dispensing needle are recorded from above. Below a critical radius $R_{2\to1}$, drops self-propel in all directions with uniform accelerations. (b) Acceleration a deduced from quadratic fits as a function of R, for plate temperatures T_p = 250°C, 350°C and 450°C. Drop mobility gets markedly enhanced below $R_{2\to1}$ (indicated with the dotted lines), the footprint for the transition from symmetric mode ($m = 2$) to asymmetric solid-like rolling mode ($m = 1$). (c) Radius $R_{2\to1}$ as a function of T_p.*

12 to 12762 ($\sigma_{1,\text{eff}}$ increased from $4 \cdot 10^{-5}$ to 1, accordingly). The stronger the flow, the more efficient the mixing. This tends to homogenize and increase the drop temperature, resulting in a decrease in ΔT. The baseflows depicted in figure 6b,c,d overestimate the experimental observations, where the velocity is typically 5 cm/s. The case $\sigma_1 = 1$ yields to unreasonable inner velocities that do not match reality, prompting us to use effective surface tension variation coefficient $\sigma_{1,\text{eff}} \leq \sigma_1$.

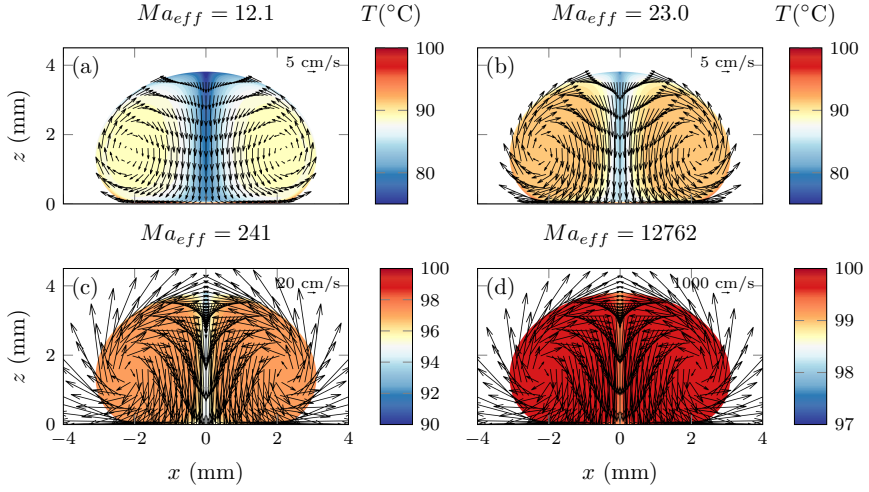

Figure 6. *Baseflow for a droplet $R = 3$ mm for different Ma_{eff}: (a) $Ma_{\text{eff}} = 12.1$ ($\sigma_{1,\text{eff}} = 4{\cdot}10^{-5}\sigma_1$), (b) $Ma_{\text{eff}} = 23.0$ ($\sigma_{1,\text{eff}} = 1{\cdot}10^{-4}\sigma_1$), (c) $Ma_{\text{eff}} = 241$ ($\sigma_{1,\text{eff}} = 3{\cdot}10^{-3}\sigma_1$) and (d) $Ma_{\text{eff}} = 12762$ ($\sigma_{1,\text{eff}} = 1 \cdot \sigma_1$). The maximum velocities are 5 cm/s, 20 cm/s, 100 cm/s and 5000 cm/s, respectively.*

The value for $\sigma_{1,\text{eff}} \leq \sigma_1$ can be assessed such that the surface tension variation gives rise to a Marangoni velocity $V \sim \sigma_1 \Delta T/(\rho_0 \nu)$ close to the reported velocities $V \approx 5$ cm/s:

$$\sigma_{1,\text{eff}} \sim \rho_0 \nu V/\Delta T \approx 5.91 \cdot 10^{-7}\,\text{N/m/K} = 3 \cdot 10^{-3}\sigma_1. \tag{16}$$

Alternatively, one could assess the effective surface tension variation $\sigma_{1,\text{eff}}$ such that the resulting temperature difference ΔT best agrees with the temperature profiles reported in figure 2 of the main manuscript. Figure 7 compares the expected surface temperature T along the boundary $\partial\Omega_F$ for R =

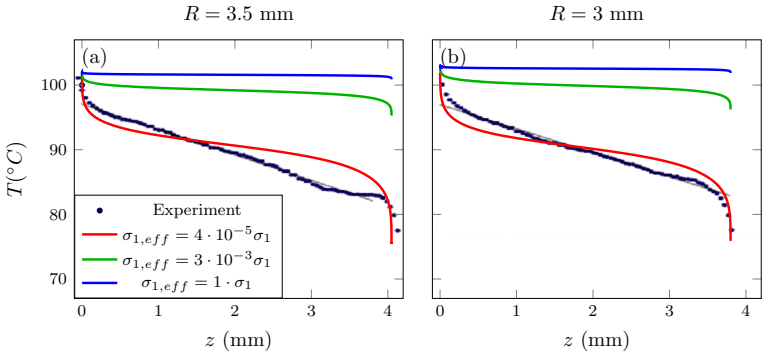

Figure 7. *Surface temperature on Leidenfrost drops with radius (a) R = 3.5 mm and (b) R = 3.0 mm as a function of the altitude z for the effective surface tension variations $4 \cdot 10^{-5}\sigma_1$, $3 \cdot 10^{-3}\sigma_1$ and $1.0 \cdot \sigma_1$. These values results in Ma_{eff} = 12.8, $2.56 \cdot 10^2$ and $1.3 \cdot 10^4$, respectively, for R = 3.5 mm and Ma_{eff} = 12.1, $2.4 \cdot 10^2$, and $1.3 \cdot 10^4$ for R = 3 mm. The altitude z, expressed in millimeter, is taken equal to zero at the drop base. Experimental data extracted from side-viewed infrared mapping of Leidenfrost puddles (taken from figure 2 in the manuscript) are showed as black dots.*

3.5 mm and 3 mm for three different values $\sigma_{1,\text{eff}}$, as compared to the experimental data (black dots, reproduced from figure 2(b) of the main article). Although none of the three curves perfectly matches in slope the experimental profiles, the curve $\sigma_{1,\text{eff}} = 4 \cdot 10^{-5}\sigma_1$ (red) best captures the experimental profiles. Moreover, the temperature difference between the top and the bottom (ΔT = 25°C) is well captured by the curve $\sigma_{1,\text{eff}} = 4 \cdot 10^{-5}\sigma_1$. The temperature difference ΔT and effective Marangoni number Ma_{eff} are summarized in table 2 for increasing $\sigma_{1,\text{eff}}$.

$\sigma_{1,\text{eff}}$	ΔT (°C)	Ma_{eff}	comments
$4 \cdot 10^{-5}\sigma_1$	26.6	12.8	chosen $\sigma_{1,\text{eff}}$
$3 \cdot 10^{-3}\sigma_1$	7.0	241	from eq. 16
$1 \cdot \sigma_1$	1.1	12762	exact
Experiment	25		

Table 2. *The temperature difference ΔT predicted in drops with radius R = 3.5 mm as a function of effective surface tension gradient $\sigma_{1,\text{eff}}$.*

8. Marangoni and Rayleigh numbers for $Ma \neq 0$

Figure 8(a,b) shows the values Ma_{eff} and Ra, using $\sigma_{1,\text{eff}} = 4 \cdot 10^{-5}\sigma_1$, as a function of the radius R (decreasing from left to right). Both numbers decrease as the radius decreases. The Marangoni number varies from 13 to 5 while the Rayleigh number does from 180000 to 8000 by changing the drop size from R =3.5 mm to 0.6 mm. Those parameters control the stability of the droplets and are also affected by the evaporation-driven size reduction. We note that the Ra number decreases faster with the droplet radius than Ma as it is a function of H^3 while Ma is proportional to H. We discuss in the manuscript

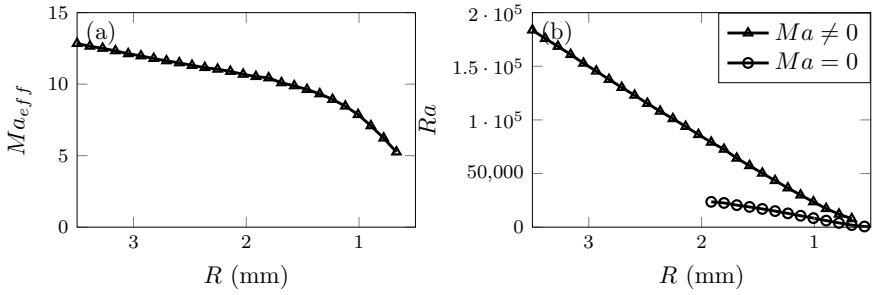

Figure 8. *The estimated (a) Ma_{eff} with $\sigma_{1,\text{eff}} = 4 \cdot 10^{-5}\sigma_1$ and (b) Ra as a function of radius of droplet. Ra when $Ma = 0$ (pure buoyancy driven) is also plotted with empty circles. The radius decreases from left to right.*

and show in Figure 4(d) the mode growth rates in the case where $Ma = 0$. The $m = 1$ mode is the only unstable mode. The corresponding Rayleigh number (for $Ma = 0, m = 1$) is plotted in figure 8(b), using dark empty circles. It decreases from 20000 to 10 as R decreases from 2 to 0.5 mm.

9. Rayleigh number for $Ma = 0$

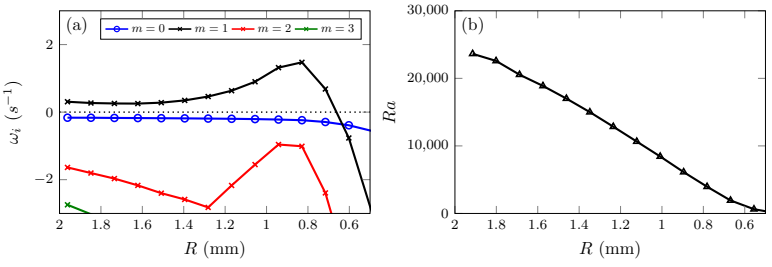

Figure 9. *(a) Growth rate for $Ma = 0$ and (b) corresponding Rayleigh number.*

Figure 9 shows the growth rate and the corresponding Rayleigh number Ra. While Ra decreases monotonically with the decrease of radii, the unstable mode $m = 1$ shows the maximum growth rate around $R \sim 1$ mm around $Ra \sim 7000$. In classical Rayleigh-Benard problem with prescribed temperature difference, Ra is an indicator of the onset of instability and the bigger Ra results in the faster growth of instability. In the Leidenfrost drop, however, as Ra is a part of the base flow solution, it may not have lost the role of indicator for the instability. One possible reason for this growth rate behaviour could be the flattened base make the rolling solution less stable. The drop base is flattened on a length that increases quadratically with R and vanishes as R decreases. That would be coherent with the stability recovery for $R < 0.8$ mm (Figure 9a).

10. Effect of heat transfer coefficient variation

In this section, the effect of the variation of evaporative (h_m) and convective (h_c) heat transfer coefficients on the base flow and stability analysis are shown. These two coefficients are evaluated by correlation laws using (7) and (14). Therefore, these values may contain some uncertainties. To access the limitation of this, a simple sensitivity analysis is conducted by changing the evaluated h_m and h_c ±20% for both base flow and the stability analysis.

Figures 10–11 show the effect of the variation of evaporative (h_m) and convective (h_c) heat transfer coefficients on the base flow. When h_m varies ±20% of the original estimated value, the base flow varies little and the estimated effective Marangoni numbers also varies ±14%. On the other hand, when the convective heat transfer coefficient h_c varies ±20%, the impact on the base flow is even lower: Ma_{eff} varies less than 1%.

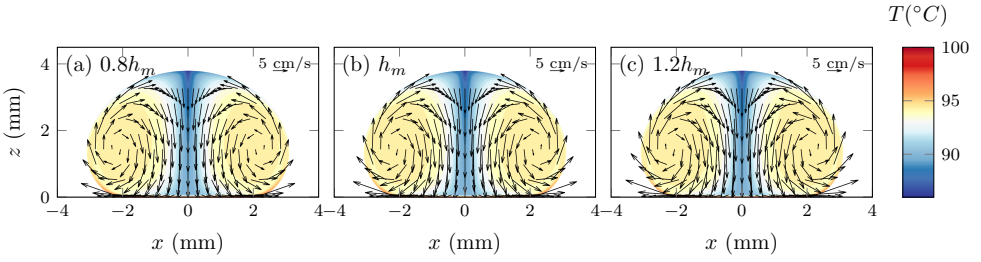

Figure 10. *Effect of evaporative heat transfer coefficient (h_m) variation on the base flow for drop R = 1.9 mm : (a) 0.8h_m, (b) h_m and (c) 1.2h_m. All other variables remained the same. The estimated Ma_{eff} for are Ma_{eff} = 10.3, Ma_{eff} = 12.1 and Ma_{eff} = 13.8, respectively.*

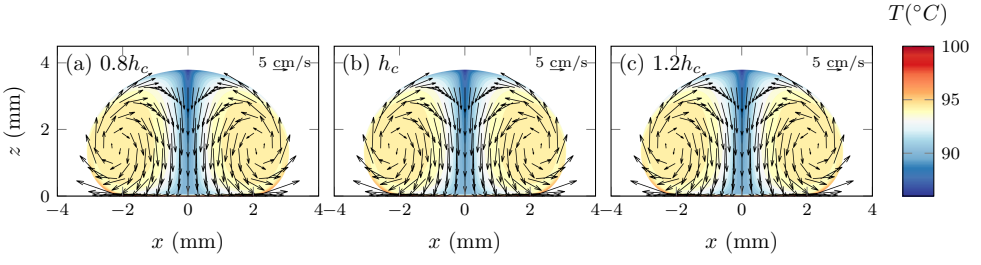

Figure 11. *Effect of convective heat transfer coefficient (h_c) variation on the base flow for drop R = 1.9 mm : (a) 0.8h_c, (b) h_c and (c) 1.2h_c. All other variables remained the same. The estimated Ma_{eff} for are Ma_{eff} = 12.2, Ma_{eff} = 12.1 and Ma_{eff} = 12.0, respectively.*

The impact on the stability analysis for example m = 1 mode is shown in Figure 12. The variation of growth rate is also limited to ∼ 10% for the variation of h_m and ∼ 1% for the variation of h_c. In summary, the variation of the heat transfer coefficients evaluated from the correlation law have slight impact on the results but does not change the major flow structures and their stability nature.

References

Bergman, T.L., Incropera, F.P., DeWitt, D.P. & Lavine, A.S. 2011 *Fundamentals of Heat and Mass Transfer*. Wiley.

Bouillant, A., Mouterde, T., Bourrianne, P., Clanet, C. & Quéré, D. 2018*a* Symmetry breaking in leidenfrost flows. *Phys. Rev. Fluids* **3** (10), 100502.

Bouillant, A., Mouterde, T., Bourrianne, P., Lagarde, A., Clanet, C. & Quéré, D. 2018*b* Leidenfrost wheels. *Nat. Phys.* **14** (12), 1188–1192.

EngineeringToolBox 2001 Available at: https://www.engineeringtoolbox.com.

Ranz, W. E. & Marshall, W. R. 1952 Evaporation from drops. *Chem. Eng. Progr* **48** (3), 141–146.

Tam, D., von Arnim, V., McKinley, G. H. & Hosoi, A. E. 2009 Marangoni convection in droplets on superhydrophobic surfaces. *J. Fluid Mech.* **624**, 101–123.

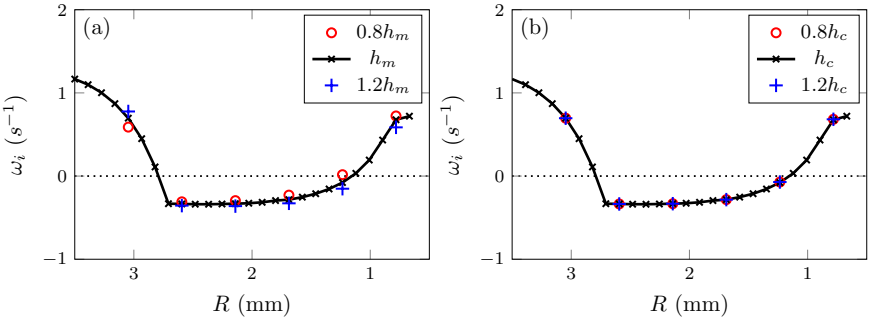

Figure 12. *Effect of (a) evaporative (h_m) and (b) convective (h_c) heat transfer coefficient variations on the growth rate for $m = 1$ for drop $R = 1.9$ mm.*

Cite this article: Yim,E. , & Bouillant,A. , & Gallaire, F. (2022). Supplementary Information: Leidenfrost Flows : instabilities and symmetry breakings. *Flow*, *0*, E1. doi:10.4153/xxxx